

Article

Symmetry Analysis of Mean Velocity Distribution in Stratified Atmospheric Surface Layers

Yong Ji ¹  and Xi Chen ^{2,*} ¹ School of Mathematics and Statistics, Ningxia University, Yinchuan 750021, China; jiyong@pku.edu.cn² Key Laboratory of Fluid Mechanics of Ministry of Education, Beihang University (Beijing University of Aeronautics and Astronautics), Beijing 100191, China

* Correspondence: chenxi97@outlook.com

Abstract: The mean velocity distributions of unstably and stably stratified atmospheric surface layers (ASLs) are investigated here using the symmetry approach. Symmetry groups for the mean momentum and the Reynolds stress equations of ASL are searched under random dilation transformations, which, with different leading order balances in different flow regions, lead to a set of specific scalings for the characteristic length ℓ_{13} (defined by Reynolds shear stress and mean shear). In particular, symmetry analysis shows that in the shear-dominated region, ℓ_{13} scales linearly with the surface height z , which corresponds to the classical log law of mean velocity. In the buoyancy-dominated region, $\ell_{13}/L \sim (z/L)^{4/3}$ for unstably stratified ASL and $\ell_{13}/L \sim const$ for stably stratified ASL, where L is the Obukhov length. The specific formula of the celebrated Monin–Obukhov similarity function is obtained, and hence an algebraic model of mean velocity profiles in ASL is derived, showing good agreement with the datum from the QingTu Lake observation array (QLOA) in China.

Keywords: atmospheric surface layer; mean velocity profile; symmetry analysis



Citation: Ji, Y.; Chen, X. Symmetry Analysis of Mean Velocity Distribution in Stratified Atmospheric Surface Layers. *Symmetry* **2023**, *15*, 1951. <https://doi.org/10.3390/sym15101951>

Academic Editor: Abraham A. Ungar

Received: 27 September 2023

Revised: 17 October 2023

Accepted: 19 October 2023

Published: 21 October 2023



Copyright: © 2023 by the authors. Licensee MDPI, Basel, Switzerland. This article is an open access article distributed under the terms and conditions of the Creative Commons Attribution (CC BY) license (<https://creativecommons.org/licenses/by/4.0/>).

1. Introduction

The atmospheric surface layer (ASL) is a specific turbulent boundary layer (TBL) in which atmosphere exchanges momentum and energy with the earth's surface through nearly constant momentum and heat flux [1]. Due to its large dimension in the horizontal and surface-normal directions, ASL typically reaches a (friction) Reynolds number of several millions [2], making it a candidate for the study of high Reynolds number canonical wall turbulence. Also, as a result of the diurnal release and absorption of the heat of the earth's surface, the turbulent flow states of ASL in the daytime and at night are significantly different [3]. Notable observation arrays, such as QLOA [4] and SLTEST (Surface Layer Turbulence and Environmental Science) [5], have been established to experimentally study the high Reynolds number properties of turbulent boundary layers [2,5–13]. Due to the limitation of grid spatial resolution, the numerical weather research and forecasting model (WRF) cannot solve the flow field in the ASL [14]. Therefore, studies on the unified description of mean velocity distribution (MVD) under various momentum and heat flux conditions are important for applications in the weather forecasting, pollutant prediction, and wind energy industry [1,3,15–17].

Since the boundary layer concept of Prandtl [18], the Monin–Obukhov (MO) similarity theory [19] has been a milestone for understanding the ASL and is regarded as the starting point of modern micrometeorology [16]. The MO theory relies on statistical stationarity and horizontal homogeneity, which results in the constant momentum and heat flux in the surface-height (or wall-normal) direction. In particular, four physical parameters are proposed in MO to depict the mean flow of the ASL: heat flux $H_w = \overline{w'T'}$, friction velocity $u_\tau = \sqrt{-\overline{u'w'}}$, buoyancy force factor g/\overline{T} , and the height z . Dimensional analysis leads to the Obukhov length scale $L = -u_\tau^3 / \left[\kappa \overline{w'T'} g / \overline{T} \right]$, where \overline{T} is the mean temperature, g is

the acceleration of gravity, κ is the von Kármán constant, and w' and T' are the fluctuating wall-normal velocity and temperature, respectively. In practical terms, L can be explained as a critical height, below which turbulence is dominated by the wall-induced shear effect, and above which it is dominated by buoyancy. Consequently, a non-dimensional similarity variable $\zeta = z/L$ is defined by MO to quantify the ratio between the shear production and buoyancy effect in the ASL. Since then, statistical quantities have all been expressed as certain functions of ζ , validated by many atmospheric experimental studies [20,21].

Particularly for the mean velocity distribution, MO proposed investigating the following dimensionless similarity function:

$$\varphi_m(\zeta) = \frac{\kappa z}{u_\tau} \frac{dU}{dz}. \quad (1)$$

To determine φ_m , an implicit function equation $\varphi_m^4 - \gamma\varphi_m^3\zeta = 1$ has been derived under an approximation of the kinetic energy balance equation, known as the O'KEYPS equation (Obukhov, Kazansky, Ellison, Yamamoto, Panofsky, and Sellers) [22]. However, the constant eddy diffusivity assumed in the O'KEYPS equation remains a subject of doubt, and the empirical parameter γ , which varies from 5 to 18 for different data sets, indicates that the form of φ_m in the O'KEYPS equation may not be universal [23].

On the other hand, based on the Kansas experimental measurements, $\varphi_m = (1 - 16\zeta)^{-1/4}$ for $\zeta < 0$ and $\varphi_m = 1 + 4.7\zeta$ for $\zeta > 0$ are well-known as the Businger–Dyer (BD) function [24,25]. However, the asymptotic scaling of BD function at the free convection limit, i.e., $\varphi_m \sim (-\zeta)^{-1/4}$ for $-\zeta \gg 1$, differs from the prediction by the O'KEYPS equation. To address this, Carl et al. [26] proposed a modified $\varphi_m = (1 - 15\zeta)^{-1/3}$, to conform with the O'KEYPS equation. Moreover, Kader and Yaglom [27] argued that in the O'KEYPS equation, $\gamma \gg 1$, as the buoyancy acts only on the direction normal to the earth's surface and hence contributes mostly to momentum transfer. They also proposed the same scaling $\varphi_m \sim (-\zeta)^{1/3}$, validated by their measured data in the top convective sublayer of the ASL [27].

More recently, Katul et al. developed a heuristic model of MVD in ASL under the attached eddy hypothesis. The characteristic velocity u_τ is derived from the assumed inertial-range spectrum, which further leads to a relation between buoyancy and momentum flux [23,28]. This model yields a similar prediction to that of the O'KEYPS equation, but it incorporates more physical considerations. For example, the large value of γ is attributed to the effects of turbulent transport, pressure redistribution, and the anisotropy of turbulent eddies. However, it should also be noted that the functional form of the similarity function becomes more complicated, and its prediction for the stable ASL deviates from observations. To account for this, Li et al. revisited Katul's model by introducing the Ozmidov scale [29] and obtained a better description of the data. Liu et al. developed an analytical model describing the vertical structure of conventionally neutral atmospheric boundary layers, providing predictions of wind and turbulent shear stress profiles [17,30]. In addition to the works mentioned, there are also efforts to extend the MO theory by further consideration of large-scale coherent structures [31], turbulence anisotropy [32], and non-zero vertical turbulent transport effects [33].

This paper aims to understand the MVD from a symmetry perspective. It is worth noting that symmetry analysis is a well-developed method for finding the similarities or invariant solutions of differential equations. A typical example is the Blasius similarity solution of a laminar boundary layer flow, the symmetry analysis of which involves three steps. First, search the dilation symmetry transformation that keeps the governing equation unchanged; second, obtain the dilation invariants for the independent and dependent variables; finally, use these invariants as variables to transfer the partial differential equation to an ordinary differential equation. When dealing with turbulence, there is a challenge in these steps because of the unknown Reynolds stresses. However, by searching the symmetry of characteristic length scales, one can construct candidate invariant solutions by

using group invariants as similarity variables. This approach has been utilized to describe turbulent mean flows in wall flows, with details provided in [34–36].

Specifically, for canonical turbulent boundary layers, a multi-layer description of the mean velocity profiles has been obtained in [34–36] through a random dilation analysis of Reynolds-averaged Navier–Stokes equations. In comparison to previous works, the novelty in [34–36] is that different leading order balances are considered in the symmetry analysis, and a general ansatz is proposed to connect the local dilation invariants. In the past few years, a large set of experimental and direct numerical simulation (DNS) data of canonical wall flows (channel, pipe, and turbulent boundary layer—TBL) have verified the multi-layer description, with successful extensions to complex boundary conditions, including pressure gradient effects, heat flux effects, and surface roughness [37,38]. Note that, as ASL is also a wall-induced shear flow, the dilation symmetry proposed in [34–36] along the wall-normal direction (z) may also exist. Thus, we plan to develop a similar modeling of the ASL in this paper based on the symmetry analysis approach.

Before proceeding further, it is important to note that a theoretical description of thermally stratified ASL flow is crucial for climate modeling of the near-surface wind fields. For instance, in the Weather Research and Forecasting (WRF) model, due to computational power cost, the WRF cannot resolve the near wall flow details. Therefore the Monin–Obukhov similarity theory (MOST) is used to estimate the exchanges of heat, momentum and humidity between the earth’s surface and the ASL. Specially for the wind speed at approximately 10 m above the earth’s surface, the accuracy of MOST is crucial for WRF predictions. Various corrections of MOST have been proposed in the WRF [14]. In this context, we present a theoretical framework for describing thermally stratified ASLs based on the symmetry approach, which offers a more comprehensive understanding compared to the models and corrections based on MOST. The results can be integrated into the WRF to enhance the prediction of near-surface wind fields.

The rest of this paper is organized as follows. The balance equations and the dilation symmetry analysis are introduced in Section 2. Section 3 introduces the experimental data, the comparison of which with our theory is provided in Section 4. Final conclusions are presented in Section 5.

2. Methods

This study is inspired by the symmetry approach for canonical TBL developed by She et al. and Chen et al. [35,36]. Note that to obtain the mean velocity distributions in ASL, one needs to address the closure problem of the unknown Reynolds shear stress. In the literature, this is usually resolved by the hypothesis of eddy viscosity or mixing length (the so-called stress length here), which builds a relation between the mean shear and Reynolds stress. However, these hypotheses have no link with the balance equations. The current paper aims to develop a procedure to determine the mixing length (or stress length) based on the balance equations. As we demonstrate below, the balance equations allow for a set of random dilations, which define the dilation invariant of the stress length. By assuming a constant dilation invariant, we can thus obtain the power-law scaling exponent for the stress length function, and hence the mean velocity distributions in ASL. Therefore, the key contribution of our paper is to present the rationale behind the scaling exponent of stress length from the symmetry consideration of the balance equations. This is reminiscent of Monin and Obukhov, who also derived the logarithmic law of wind distribution based on the concept of dilation symmetry [19]. However, our approach contains more mathematical details and extends to different flow regions.

The ensemble averaged momentum and Reynolds stresses equations are [27,36]

$$\frac{\partial \overline{-u'w'}}{\partial z} + \nu \frac{\partial^2 U}{\partial z^2} = 0, \quad (2)$$

$$\underbrace{\overline{-u'w'}}_{SP} \frac{\partial U}{\partial z} + \underbrace{\overline{p'}}_{R_u} \frac{\partial u'}{\partial x} - \underbrace{\frac{1}{2} \overline{\partial u'^2 w'}}_{T_u} \frac{\partial U}{\partial z} - \underbrace{\nu \overline{|\nabla u'|^2}}_{\epsilon_u} + \underbrace{\nu \frac{\partial^2}{\partial z^2} \left(\frac{1}{2} \overline{u'^2} \right)}_{D_u} = 0, \quad (3)$$

$$\underbrace{\overline{p'}}_{R_v} \frac{\partial v'}{\partial y} - \underbrace{\frac{1}{2} \overline{\partial v'^2 w'}}_{T_v} \frac{\partial v'}{\partial z} - \underbrace{\nu \overline{|\nabla v'|^2}}_{\epsilon_v} + \underbrace{\nu \frac{\partial^2}{\partial z^2} \left(\frac{1}{2} \overline{v'^2} \right)}_{D_v} = 0, \quad (4)$$

$$\underbrace{\overline{w'T'}}_B \frac{g}{T} + \underbrace{\overline{p'}}_{R_w} \frac{\partial w'}{\partial z} - \underbrace{\frac{1}{2} \overline{\partial w'^3 + 2p'w'}}_{T_w} \frac{\partial w'}{\partial z} - \underbrace{\nu \overline{|\nabla w'|^2}}_{\epsilon_w} + \underbrace{\nu \frac{\partial^2}{\partial z^2} \left(\frac{1}{2} \overline{w'^2} \right)}_{D_w} = 0, \quad (5)$$

$$-\frac{1}{2} \overline{w'w'} \frac{\partial U}{\partial z} - \frac{1}{2} \overline{u'p'} \frac{\partial p'}{\partial z} - \frac{1}{2} \overline{w'p'} \frac{\partial p'}{\partial x} - \frac{1}{2} \overline{\partial u'w'w'} \frac{\partial U}{\partial z} - \nu \overline{|\nabla u' \bullet \nabla w'|} + \nu \frac{\partial^2}{\partial z^2} \left(\frac{1}{2} \overline{u'w'} \right) = 0, \quad (6)$$

where overline denotes the time-spatial ensemble average; p' is the pressure fluctuation and u', w', v' are the streamwise, vertical (or surface-height), and spanwise velocity fluctuations with U the mean streamwise velocity; SP is the shear production; $R_{u,w,v}$ are pressure redistribution terms; $T_{u,w,v}$ are vertical spatial turbulent transports; $\epsilon_{u,w,v}$ are turbulent dissipation rates; $D_{u,w,v}$ are diffusion terms; subscript u, w, v denote three velocity fluctuation components.

The above equations for ASL are similar to the canonical boundary layer flows except for the additional buoyancy term (i.e., the heat flux) $B = \overline{w'T'g}/\overline{T}$ in Equation (5). The buoyancy term could be an energy source for upward heat flux ($B > 0$), or a sink for downward heat flux ($B < 0$). Since the shear production (SP) decreases as z^{-1} and the buoyancy (B) is invariant as the height Z increases, the shear production dominates the balance equations for small z while the buoyancy dominates for large z . As shown below, the alteration of dominant balance would result in different dilation transformations, leading to different scalings in different flow regions.

To proceed, normalizing the above Equations (2)–(6) by the friction velocity u_τ , the wall heat flux H_w , and the Obukhov length L yields

$$\frac{\partial \overline{-u'^+w'^+}}{\partial \zeta_z} + \frac{1}{L^+} \frac{\partial^2 U^+}{\partial \zeta_z^2} = 0, \quad (7)$$

$$\underbrace{\overline{-u'^+w'^+}}_{SP^+} \frac{\partial U^+}{\partial \zeta_z} + \underbrace{\overline{p'^+}}_{R_u^+} \frac{\partial u'^+}{\partial \zeta_x} - \underbrace{\frac{1}{2} \overline{\partial u'^+2w'^+}}_{T_u^+} \frac{\partial U^+}{\partial \zeta_z} - \underbrace{\frac{1}{L^+} \overline{|\nabla_L u'^+|^2}}_{\epsilon_u^+} + \underbrace{\frac{1}{L^+} \frac{\partial^2}{\partial \zeta_z^2} \left(\frac{1}{2} \overline{u'^+2} \right)}_{D_u^+} = 0, \quad (8)$$

$$\underbrace{\overline{p'^+}}_{R_v^+} \frac{\partial v'^+}{\partial \zeta_y} - \underbrace{\frac{1}{2} \overline{\partial v'^+2w'^+}}_{T_v^+} \frac{\partial v'^+}{\partial \zeta_z} - \underbrace{\frac{1}{L^+} \overline{|\nabla_L v'^+|^2}}_{\epsilon_v^+} + \underbrace{\frac{1}{L^+} \frac{\partial^2}{\partial \zeta_z^2} \left(\frac{1}{2} \overline{v'^+2} \right)}_{D_v^+} = 0, \quad (9)$$

$$\underbrace{\overline{w'^+T'^+}}_B + \underbrace{\overline{p'^+}}_{R_w^+} \frac{\partial w'^+}{\partial \zeta_z} - \underbrace{\frac{1}{2} \overline{\partial w'^+3 + 2p'^+w'^+}}_{T_w^+} \frac{\partial w'^+}{\partial \zeta_z} - \underbrace{\frac{1}{L^+} \overline{|\nabla_L w'^+|^2}}_{\epsilon_w^+} + \underbrace{\frac{1}{L^+} \frac{\partial^2}{\partial \zeta_z^2} \left(\frac{1}{2} \overline{w'^+2} \right)}_{D_w^+} = 0, \quad (10)$$

$$-\frac{1}{2} \overline{w'^+w'^+} \frac{\partial U^+}{\partial \zeta_z} - \frac{1}{2} \overline{u'^+p'^+} \frac{\partial p'^+}{\partial \zeta_z} - \frac{1}{2} \overline{w'^+p'^+} \frac{\partial p'^+}{\partial \zeta_x} - \frac{1}{2} \overline{\partial u'^+w'^+w'^+} \frac{\partial U^+}{\partial \zeta_z} - \frac{1}{L^+} \overline{|\nabla_L u'^+ \bullet \nabla_L w'^+|} + \frac{1}{L^+} \frac{\partial^2}{\partial \zeta_z^2} \left(\frac{1}{2} \overline{u'^+w'^+} \right) = 0, \quad (11)$$

where superscript plus + means being normalized by wall variables, i.e.,

$$[u'^+, v'^+, w'^+, U^+, p'^+, L^+, T'^+] = \left[\frac{u'}{u_\tau}, \frac{v'}{u_\tau}, \frac{w'}{u_\tau}, \frac{U}{u_\tau}, \frac{p'}{u_\tau^2}, \frac{L}{\nu/u_\tau}, \frac{T'}{\kappa H_w/u_\tau} \right],$$

and $\nabla_L = \partial/\partial\zeta_x + \partial/\partial\zeta_y + \partial/\partial\zeta_z$ is gradient operator, with $\zeta_x = x/L$, $\zeta_y = y/L$, and $\zeta_z \equiv \zeta = z/L$.

Following the step in [35,36], we define the Reynolds shear stress length function $\ell_{13}^\wedge = \frac{\sqrt{-u'^+w'^+}}{\partial U^+/\partial \zeta}$, which characterizes the size of eddies responsible for vertical momentum transport. This enables us to solve the mean velocity profile from Equation (7):

$$U^+(h/L) = \int_{h_0/L}^{h/L} \frac{\sqrt{-u'^+w'^+}}{\ell_{13}^\wedge} d\zeta. \tag{12}$$

Here, h is the height of interest, h_0 is the typical roughness height, and $\ell_{13}^\wedge = \ell_{13}/L$ with $\ell_{13} = \frac{\sqrt{-u'w'}}{\partial U/\partial z}$. Note that ASL is a constant momentum flux layer, which means $-u'^+w'^+ = 1$; hence, Equation (12) is written

$$U(h) = u_\tau \int_{h_0}^h \frac{dz}{\ell_{13}}. \tag{13}$$

Once ℓ_{13} is known, the mean velocity $U(h)$ can also be determined.

To obtain the formula of ℓ_{13} , a random dilation transformation [36] is introduced as follows:

$$\zeta_i^* = q_i \zeta_i, \quad U^* = \lambda_U U, \quad L^* = \lambda_L L, \quad u_i'^* = \lambda_i u_i', \quad p'^* = \lambda_p p', \quad T'^* = \lambda_T T', \tag{14}$$

where q_i and λ_U, λ_L are regular dilation factors, while λ_i, λ_p , and λ_T are random factors with zero means; and $i = (1, 2, 3)$ denotes (x, y, z) . Note that superscript '+' is neglected here. Substituting (14) into the balance Equations (7)–(11), the symmetry requires that equations under dilation remain invariant, which leads to the following relationships among dilation parameters:

$$\frac{\overline{\lambda_1 \lambda_3}}{q_3} = \frac{1}{\lambda_L} \frac{\lambda_U}{q_3^2}, \tag{15}$$

$$\overline{\lambda_1 \lambda_3} \frac{\lambda_U}{q_3} = \frac{\overline{\lambda_p \lambda_1}}{q_1} = \frac{\overline{\lambda_1 \lambda_1 \lambda_3}}{q_3} = \frac{1}{\lambda_L} \frac{\overline{\lambda_1 \lambda_1}}{q_1^2} = \frac{1}{\lambda_L} \frac{\overline{\lambda_1 \lambda_1}}{q_2^2} = \frac{1}{\lambda_L} \frac{\overline{\lambda_1 \lambda_1}}{q_3^2}, \tag{16}$$

$$\frac{\overline{\lambda_p \lambda_2}}{q_2} = \frac{\overline{\lambda_2 \lambda_2 \lambda_3}}{q_3} = \frac{1}{\lambda_L} \frac{\overline{\lambda_2 \lambda_2}}{q_1^2} = \frac{1}{\lambda_L} \frac{\overline{\lambda_2 \lambda_2}}{q_2^2} = \frac{1}{\lambda_L} \frac{\overline{\lambda_2 \lambda_2}}{q_3^2}, \tag{17}$$

$$\overline{\lambda_3 \lambda_T} = \frac{\overline{\lambda_p \lambda_3}}{q_3} = \frac{\overline{\lambda_3 \lambda_3 \lambda_3}}{q_3} = \frac{1}{\lambda_L} \frac{\overline{\lambda_3 \lambda_3}}{q_1^2} = \frac{1}{\lambda_L} \frac{\overline{\lambda_3 \lambda_3}}{q_2^2} = \frac{1}{\lambda_L} \frac{\overline{\lambda_3 \lambda_3}}{q_3^2}, \tag{18}$$

$$\overline{\lambda_3 \lambda_3} \frac{\lambda_U}{q_3} = \frac{\overline{\lambda_p \lambda_1}}{q_3} = \frac{\overline{\lambda_p \lambda_3}}{q_1} = \frac{\overline{\lambda_1 \lambda_3 \lambda_3}}{q_3} = \frac{1}{\lambda_L} \frac{\overline{\lambda_1 \lambda_3}}{q_1^2} = \frac{1}{\lambda_L} \frac{\overline{\lambda_1 \lambda_3}}{q_2^2} = \frac{1}{\lambda_L} \frac{\overline{\lambda_1 \lambda_3}}{q_3^2}. \tag{19}$$

An important fact is that in different flow regions, there are different leading order balances in (7)–(11) so that we can define a locally valid dilation group by neglecting unimportant terms. This provides extra freedoms for the group parameters in Equations (15)–(19), as practised below in different flow layers.

2.1. Homogeneous Dilations in the Shear Dominated Layer

In the shear dominated layer, the shear production (SP) is balanced by dissipation from all three spatial directions. Hence, all the spatial derivatives in (3)–(6) are important, leading to a homogeneous dilation in three directions, i.e., $q_1 = q_2 = q_3 = q$ in (15)–(19). Furthermore, from $\overline{\lambda_1 \lambda_3} \frac{\lambda_U}{q} = \frac{\overline{\lambda_p \lambda_1}}{q} = \frac{1}{\lambda_L} \frac{\overline{\lambda_1 \lambda_3}}{q^2}$, we obtain $\lambda_U \lambda_L = q^{-1}$; considering $\overline{\lambda_3 \lambda_T} = 1$ for constant heat flux, from Equations (15), (18), and (19), we obtain $\lambda_L^2 / \lambda_U = q^{-3}$, and hence

$$\lambda_L = q^{-4/3}, \quad (20)$$

$$\lambda_U = q^{1/3}, \quad (21)$$

$$\overline{\lambda_1 \lambda_1} = \overline{\lambda_1 \lambda_3} = \overline{\lambda_3 \lambda_3} = q^{2/3}, \quad (22)$$

$$\overline{\lambda_p \lambda_1} = \overline{\lambda_p \lambda_3} = \overline{\lambda_1 \lambda_1 \lambda_3} = \overline{\lambda_2 \lambda_3 \lambda_3} = \overline{\lambda_3 \lambda_3 \lambda_3} = q. \quad (23)$$

Therefore, the dilation factor for length function ℓ_{13}^\wedge is

$$\lambda_{13} = \frac{\overline{\lambda_1 \lambda_3}^{-1/2}}{\lambda_U/q} = \frac{q^{1/3}}{q^{1/3}/q} = q, \quad (24)$$

whose corresponding dilation invariant is

$$I_{13} = \frac{\ell_{13}^\wedge}{\zeta}. \quad (25)$$

It is a normal result that length function takes its ordinary dimension if no direction is preferred, the same as the classical dimensional analysis result. In [36], the dilation invariant for stress length is found to be $I_{13} = 0.45$, and hence $\ell_{13}^\wedge = 0.45\zeta$ for canonical boundary layer flows. In ASL, the value of I_{13} may slightly change, but the functional form is the same.

2.2. Inhomogeneous Dilation in the Convective Layer ($B > 0$)

Let us consider the region where height $z > L$ and $B > 0$, and hence the buoyancy term overtakes the shear production to balance dissipation in Equations (16)–(18). Subsequently, the shear production and turbulent transport terms could be neglected in Equations (16)–(18). On the other hand, in the Reynolds shear stress Equation (11) or (19), the dominant balance is still between the first term of production and the fifth term of dissipation. Based on these considerations, Equations (15), (18) and (19) could be, respectively, simplified to

$$\frac{\overline{\lambda_1 \lambda_3}}{q} = \frac{1}{\lambda_L} \frac{\lambda_U}{q^2}, \quad (26)$$

$$\overline{\lambda_3 \lambda_T} = \frac{1}{\lambda_L} \frac{\overline{\lambda_3 \lambda_3}}{q^2}, \quad (27)$$

$$\overline{\lambda_3 \lambda_3} \frac{\lambda_U}{q} = \frac{1}{\lambda_L} \frac{\overline{\lambda_1 \lambda_3}}{q^2}. \quad (28)$$

Furthermore, considering that momentum and heat flux are constant in the buoyancy dominant layer, we obtain $\overline{\lambda_3 \lambda_T} = 1$ and $\overline{\lambda_1 \lambda_3} = 1$, and hence $\lambda_U = q^{-1/3}$, $\lambda_T = q^{-4/3}$ and $\overline{\lambda_3 \lambda_3} = q^{2/3}$. Thus, the dilation factor of ℓ_{13}^\wedge is

$$\lambda_{13} = \frac{1}{\lambda_U/q} = q^{4/3}. \quad (29)$$

Therefore, in the convective layer, the stress length satisfies $\ell_{13}^\wedge \propto \zeta^{4/3}$.

2.3. Inhomogeneous Dilation in the Stably Stratified Layer ($B < 0$)

When $B < 0$, buoyancy, acting as a sink, would absorb kinetic energy. Hence, the dominant balance for the Reynolds normal stresses are between SP and B (instead of dissipation). In other words, when summing Equations (8)–(10) all together, the balance is between SP and B. Under this condition, the dilation parameters are simplified to be

$$\overline{\lambda_3 \lambda_T} = \overline{\lambda_1 \lambda_3} \frac{\lambda_U}{q}. \quad (30)$$

Again, as $\overline{\lambda_3 \lambda_T} = 1$ and $\overline{\lambda_1 \lambda_3} = 1$, we obtain $\lambda_U = q$. Therefore, the dilation parameter of ℓ_{13} is

$$\lambda_{13} = \frac{1}{\lambda_U/q} = 1, \quad (31)$$

which means that ℓ_{13}^\wedge is a constant.

2.4. Composite Formula of ℓ_{13}^\wedge in ASL

According to the dilation analysis above, the scaling of ℓ_{13}^\wedge in different flow layers is obtained. Following the same matching procedure introduced in [35], a two-layer formula of stress length connecting the adjacent power-law scalings can be obtained:

$$\ell_{13}^\wedge \propto \begin{cases} \zeta \left(1 - \frac{\zeta}{\zeta_{UC}}\right)^{1/3}, & \zeta < 0 \\ \zeta \left(1 + \frac{\zeta}{\zeta_{SC}}\right)^{-1}, & \zeta > 0 \end{cases}. \quad (32)$$

Here, ζ_{UC} and ζ_{SC} are empirical parameters to be determined from data. In [33], they are given as $\zeta_{UC} = 1/6.3$ and $\zeta_{SC} = 1/2$, respectively. For ζ below the critical height ζ_{UC} and ζ_{SC} , the linear scaling of ℓ_{13}^\wedge is consistent with wall-attached eddy size in the log layer [39]. For ζ above ζ_{UC} , the scaling $\zeta^{4/3}$ for unstably stratified ASL indicates that the momentum transport eddies are stretched in the vertical direction by the buoyancy force. On the contrary, for stably stratified ASL, the buoyancy force depresses eddy size in a vertical direction, resulting in a finite value of ℓ_{13}^\wedge .

2.5. Composite Formula of ϕ_m in ASL

According to the definitions of ϕ_m and ℓ_{13} , we obtain the relation between ϕ_m and ℓ_{13} as:

$$\phi_m(\zeta) = \frac{\sqrt{-u'w'}}{\ell_{13}} \times \frac{\kappa z}{u_\tau}. \quad (33)$$

Considering that $\sqrt{-u'w'}/u_\tau = 1$, we have

$$\phi_m \propto \begin{cases} (1 - \zeta/\zeta_{UC})^{-1/3}, & \zeta < 0 \\ 1 + \zeta/\zeta_{SC}, & \zeta > 0 \end{cases}. \quad (34)$$

3. Data

Data collected for the verification of our derivations include the Kansas measurements, the AHATS (advection horizontal array turbulence study) measurements, and the QLOA measurements. AHATS investigated surface-layer turbulence in the San Joaquin Valley, California, during the summer of 2008, while details on Kansas and AHATS are referred to references [24,40].

For QLOA, it is conducted on the dry lake bed located in Minqin County, Gansu Province, in the northwestern region of China. QLOA has one main tower that is 32 m high, surrounded by twenty lower towers that are 5 m high and shaped like the character 'T'. Data measured from the main tower are examined here, which are acquired from eleven sonic anemometers. Wind speed vectors and virtual temperature are sampled at a frequency of 50 Hz. QLOA has collected day and night data lasting about ten years, covering various weather conditions, and has been used to study the large-scale motion, energy spectrum, amplitude modulation between multi-scale turbulent motions, and two-phase flows during sand storms [4,41,42]. The observations of QLOA are divided into time-ensemble blocks of 1 h. This study uses 12 sets of unstably stratified data and 11 sets of stably stratified data, with details shown in Table 1. The pretreatment of the data is conducted to transform wind signals into a streamwise direction [4]. The friction velocity u_τ is estimated using Reynolds shear stress, $u_\tau = \sqrt{\sum_{i=1}^{11} \langle -u'w' \rangle_i / 11}$. Here i denotes sonic

anemometer at various heights and $\langle * \rangle_i$ means averaging one hour at i th height. Similarly, the wall heat flux is estimated by $H_w = \sum_{i=1}^{11} \langle w'T' \rangle_i / 11$. To obtain shear production, dU/dz is calculated from mean velocity data using the log-polynomial fitting [43], specifically, $U = c_0 + c_1 \log z + c_2 (\log z)^2$. At each height z , five adjacent points are used to determine the coefficients c_0 , c_1 , and c_2 , so that $dU/dz = c_1/z + 2c_2 \log z/z$. The turbulent dissipation rate is estimated using $\epsilon \approx \frac{1}{K_1 - K_0} \int_{K_0}^{K_1} (E_{11}(k)k^{5/3}/C_{11})^{3/2} dk$, where E_{11} is the spectrum of streamwise velocity fluctuation, $C_{11} = 0.5$ is the longitudinal Kolmogorov constant, while K_0 and K_1 indicate the start and the end of the Kolmogorov initial range, and wavenumber k is calculated from frequency and local mean velocity by using the Taylor freezing hypothesis, $k = 2\pi f/U$ [44].

Table 1. The information of QLOA data used in this paper.

No.	Time and Date	u_τ (m/s)	H_w (K·m/s)	L (m)
1	2014-5-23 7:00–8:00	0.28	0.016	−96.4
2	2014-5-23 8:00–9:00	0.31	0.087	−22.8
3	2014-5-23 9:00–10:00	0.32	0.155	−13.5
4	2014-5-23 10:00–11:00	0.33	0.203	−11.4
5	2014-5-23 11:00–12:00	0.34	0.222	−11.4
6	2014-5-23 12:00–13:00	0.29	0.209	−7.7
7	2014-5-23 13:00–14:00	0.33	0.230	−10.4
8	2014-5-23 14:00–15:00	0.29	0.279	−6.1
9	2014-5-23 15:00–16:00	0.30	0.180	−9.8
10	2014-5-23 16:00–17:00	0.34	0.161	−16.9
11	2014-5-23 17:00–18:00	0.39	0.147	−27.2
12	2014-5-23 18:00–19:00	0.35	0.080	−36.8
13	2014-3-27 0:00–1:00	0.26	−0.036	31.0
14	2014-3-27 1:00–2:00	0.59	−0.057	237.6
15	2014-3-27 2:00–3:00	0.67	−0.055	351.0
16	2014-3-27 3:00–4:00	0.59	−0.039	350.5
17	2014-3-27 4:00–5:00	0.48	−0.026	263.9
18	2014-3-27 5:00–6:00	0.41	−0.018	259.4
19	2014-3-27 6:00–7:00	0.31	−0.014	134.9
20	2014-3-27 7:00–8:00	0.25	−0.007	143.8
21	2014-5-23 2:00–3:00	0.22	−0.025	27.5
22	2014-5-23 6:00–7:00	0.21	−0.013	47.2
23	2014-5-23 20:00–21:00	0.23	−0.019	40.6

4. Results

In Section 2, we demonstrate that different leading order balances of the budget equations lead to different dilation symmetries. However, due to a scarcity of data, it is impossible to check every equation for Reynolds stresses. To address this, we sum together Equations (3)–(5) and obtain the turbulent kinetic energy equation (TKE), which could also be used to verify the leading order balances in different flow conditions. Accordingly, Figure 1 shows the wall-normal (or surface-normal) variation of shear production (SP), buoyancy effect (B), dissipation rate (ϵ), and all other terms (including pressure and spatial transport effects) as the residue (i.e., $SP + B - \epsilon$). In particular, Figure 1a presents the neutrally stratified ASL where heat flux is small and the Obukhov length L is about -96.4 m. It is clear that for lower heights (e.g., $z < 10$ m), the dominant balance is between the shear production and dissipation, which is consistent with the analysis in Section 2.1. Conversely, for $z > 10$ m, the residue is comparable with the dissipation, but the buoyancy term is always smaller than others, hence indicating the neutral stratification condition.

In contrast, Figure 1b shows the unstably stratified case in which $L = -6.1$ m. While the dominant balance is between the shear production and the dissipation for $z < 1$ m, the heat flux is much larger than the neutral case. For $z > 5$ m, the heat flux is comparable to the dissipation and the shear production, indicating a strong buoyancy effect that plays a role as an energy source—consistent with the analysis in Section 2.2. Meanwhile,

the pressure and transport effect (indicated by the residue) is negative, drawing out the local kinetic energy to other flow regions.

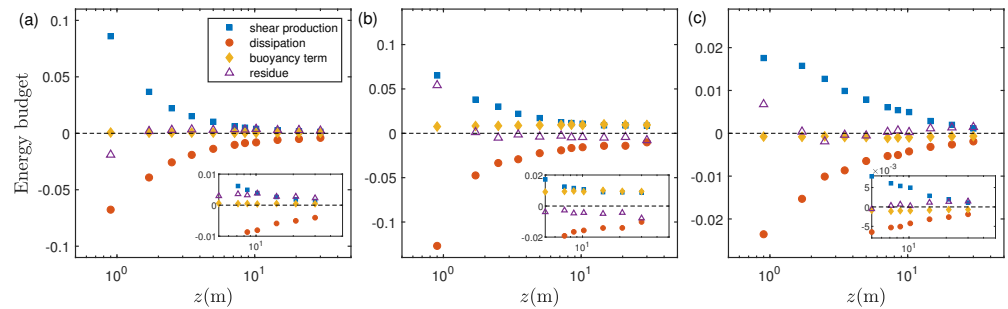


Figure 1. The measured TKE budget in QLOA for neutrally (a), unstably (b) and stably (c) stratified ASL. The inset shows TKE budget for $z > 5$ m.

Moreover, the TKE budget for the stably stratified ASL is shown in Figure 1c for which $L = 27.5$ m. It is obvious that when $z < 20$ m, the shear production and dissipation are the two dominant terms. However, for $z > 20$ m, the shear production, buoyancy effect, dissipation, and the transport effect are all comparable with each other. The notable point is that the buoyancy term B is negative (consistent with the analysis in Section 2.3), indicating that it drains out flow energy as the role of dissipation ϵ , a distinct feature for the stably stratified condition.

Therefore, different leading order balances specified in the above Section 2 have all been verified by ASL data. Now, let us validate the scaling of stress length derived in Section 2. Figure 2 shows the comparison between Equation (32) and the data, with panel (a) for the stable stratification and (b) for the unstable stratification of ASL. Note that ϕ_m are extracted from Kansas and AHATS data and then translated to ℓ_{13} using $\ell_{13} = \kappa z / \phi_m$. Dashed lines indicate the linear scaling, while solid lines are Equation (32) derived from our symmetry analysis. For $|\zeta| = |z/L| < 0.1$, the stress length ℓ_{13}^\wedge displays a linear variation (dashed line), indicating the dominance of the shear production and hence the log-law of mean velocity. However, for large $|\zeta|$, ℓ_{13}^\wedge deviates from linear behavior. On the one hand, for stable stratification in Figure 2a, ℓ_{13}^\wedge tends to be a constant. A close examination of the data shows the best fit of $\ell_{13}^\wedge = 0.35\zeta(1 + 2.0\zeta)^{-1}$ for QLOA measurements, while $\ell_{13}^\wedge = 0.35\zeta(1 + 4.0\zeta)^{-1}$ for the Kansas and AHATS measurements. The different value of $\zeta_{SC} = 0.5$ for QLOA compared to $\zeta_{SC} = 0.25$ for Kansas and AHATS is understandable because a non-zero pressure and spatial transport effect may bring in different heat flux, subsequently altering ζ_{SC} . Such a point has been observed and explained in [33]. On the other hand, as shown in Figure 2b for the unstable stratification case, all the data from QLOA, Kansas, and AHATS align nicely. They follow the trend of Equation (32) with $\ell_{13}^\wedge = 0.40\zeta(1 - 6.3\zeta)^{1/3}$, which is a general expression for the unstable stratification of ASL.

Finally, the mean velocity profile is obtained using Equation (13) with the stress length provided in Equation (32). While MVD data of Kansas and AHATS measurements are not available, the comparison is presented here only for the QLOA measurements, as shown in Figure 3. In total, there are twelve mean velocity profiles presented here; they are measured in different time. At $h = 30$ m (the highest data point for experimental observation), the friction Reynolds number $Re_{30m} = \frac{30 \text{ m} * u_\tau}{\nu}$ is calculated, along with the value of the Obukhov length L , both marked on top of the labels for each of the subplots. Notably, subplots (a), (g), and (h) pertain to the neutrally stratified ASL indicated by the very large value of $|L|$, approximately 100 m. The latter condition means that most of the data points are measured in the flow region $|z/L| < 0.1$, in which buoyancy is insignificant. Moreover, subplots (b), (c), (d), (e), and (f) are for unstably stratified ASL, where the heat flux is upward and L is negative. The rest of the subplots are for stably stratified ASL where L is positive. The dashed lines in Figure 3 indicate the log-law, which agrees with most flow data for neutrally stratified cases (subplots (a), (g), and (h)), but only depicts data

at small z for other flow cases. The red lines in Figure 3 indicate the predictions using $\ell_{13}^\wedge = 0.35\zeta(1 + 2.0\zeta)^{-1}$ for unstable cases, while blue lines indicate the predictions using $\ell_{13}^\wedge = 0.40\zeta(1 - 6.3\zeta)^{1/3}$ for stable cases. It is evident that data deviation from the log-law is well captured by the formula of ℓ_{13} derived from our symmetry analysis.

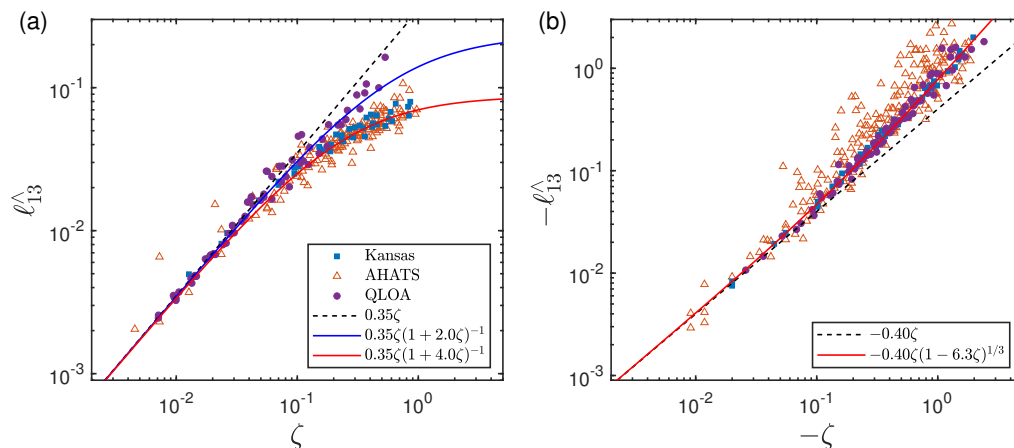


Figure 2. The normalized stress length $\ell_{13}^\wedge = \ell_{13}/L$ for stably (a) and unstably (b) stratified ASL. Circles are QLOA measurements; squares are Kansas experimental data [24], and triangles are AHATS experimental data [40].

It should be mentioned that, to obtain the mean velocity profile, an integration parameter h_0 is needed in Equation (13), which indicates the surface roughness height in QLOA. According to our study, we find that h_0 varies slightly for the above twelve mean velocity profiles. That is, for subplots (a)–(f), $h_0 = (0.08, 0.23, 0.57, 0.42, 0.32, 0.20)$ mm; for subplots (g)–(l), $h_0 = (0.60, 0.20, 0.28, 1.30, 1.60, 1.90)$ mm. The mechanism for the slight variation of these h_0 heights deserves future studies.

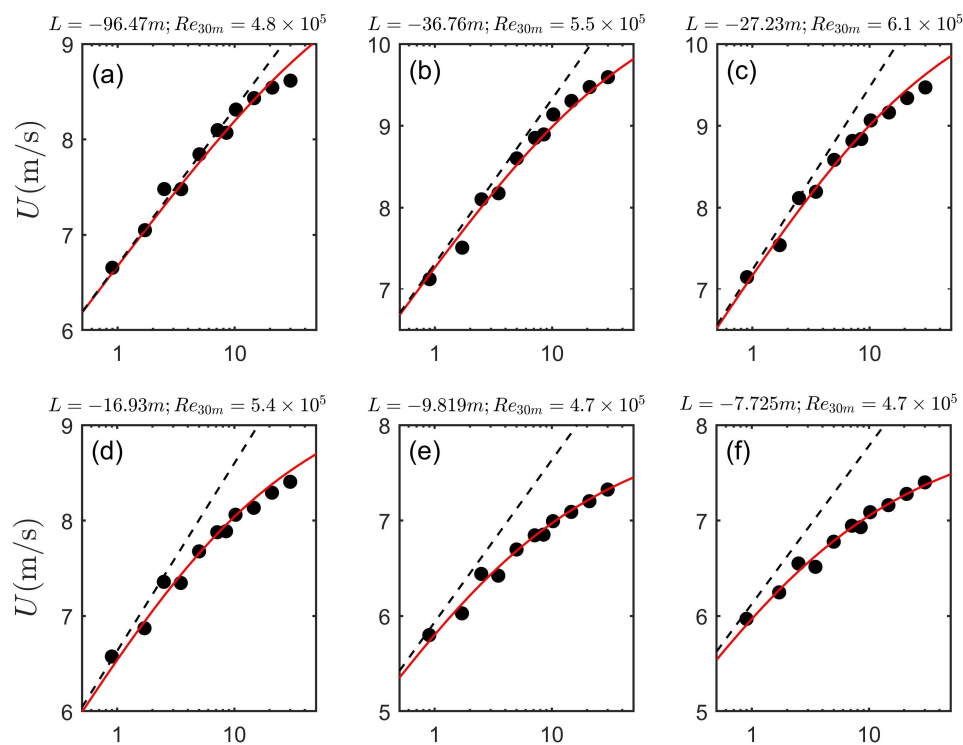


Figure 3. Cont.

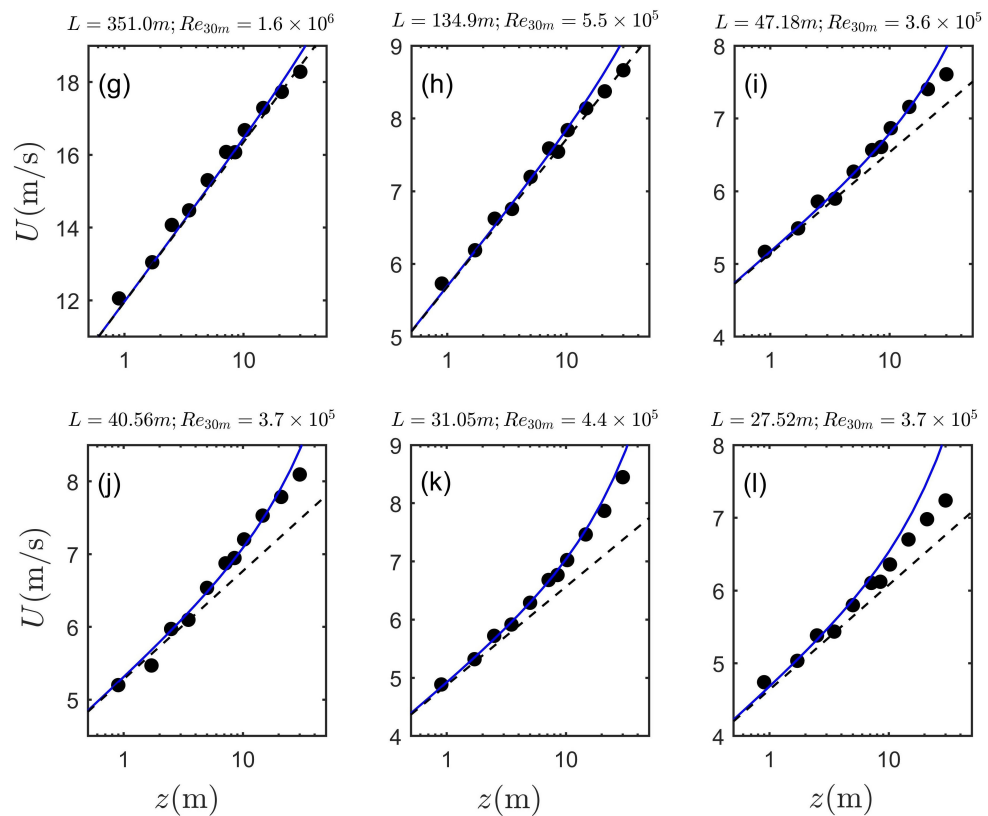


Figure 3. Mean velocity distributions measured in QLOA for neutrally (a,g,h), unstably (b–f), and stably (i–l) stratified ASL. Dashed lines indicate the log-law; solid lines are given by Equation (13) provided with Equation (32).

5. Conclusions

The symmetry approach developed for canonical wall turbulence [35,36] has now been extended to describe the mean velocity distribution in the stratified atmospheric surface layer. By performing the random dilation on the governing equations and further considerations on different leading order balances, the scaling of Reynolds stress length is specified in different flow layers. That is, in the shear-dominated log layer, $\ell_{13} \propto \zeta$; in the buoyancy dominated layer, $\ell_{13} \propto \zeta^{4/3}$ for unstably stratified ASL while a constant ℓ_{13} for stably stratified ASL. Using the matching procedure in [35,36], a composite formula of ℓ_{13} is obtained, i.e., $0.40\zeta(1 - 6.3\zeta)^{1/3}$ for unstable stratification and $0.35\zeta(1 + 2.0\zeta)^{-1}$ for stable stratification, which leads to a close representation for the mean velocity distributions measured in QLOA.

It should be noted that the linear coefficients are 0.40 for unstable stratification and 0.35 for stable stratification. Additionally, the value of $\zeta_{UC,SC}$ cannot be explained by the symmetry view. More effort should be devoted to determining these values from a theoretical perspective. Furthermore, the symmetry approach can also be applied to describe the intensity profiles in the streamwise, wall-normal, and spanwise directions, which will be investigated in the future.

Author Contributions: Conceptualization, Y.J. and X.C.; methodology, Y.J.; software, Y.J.; validation, Y.J.; formal analysis, Y.J.; investigation, Y.J.; resources, Y.J.; data curation, Y.J.; writing—original draft preparation, Y.J. and X.C.; writing—review and editing, Y.J. and X.C.; visualization, Y.J.; supervision, X.C.; project administration, X.C.; funding acquisition, X.C. All authors have read and agreed to the published version of the manuscript.

Funding: X. Chen acknowledges the support by the National Natural Science Foundation of China, No. 12072012, 92252201 and 91952302, and “the Fundamental Research Funds for the Central Universities”.

Data Availability Statement: There is no new data used in this study.

Acknowledgments: The authors thank Zhen-Su She for helpful comments and suggestions at the early stage of this study. The authors also thank Xiaojing Zheng and Guohua Wang for sharing the QLOA data with us and for many helpful discussions.

Conflicts of Interest: The authors declare no conflict of interest.

References

1. Panofsky, H.A. The Atmospheric Boundary Layer Below 150 Meters. *Annu. Rev. Fluid Mech.* **1974**, *6*, 147–177. [[CrossRef](#)]
2. Marusic, I.; Mathis, R.; Hutchins, N. Predictive model for wall-bounded turbulent flow. *Science* **2010**, *329*, 193–196. [[CrossRef](#)] [[PubMed](#)]
3. Monin, A.S. The Atmospheric Boundary Layer. *Annu. Rev. Fluid Mech.* **1970**, *2*, 225–250. [[CrossRef](#)]
4. Wang, G.; Zheng, X. Very large scale motions in the atmospheric surface layer: A field investigation. *J. Fluid Mech.* **2016**, *802*, 464–489. [[CrossRef](#)]
5. Klewicki, J.C.; Foss, J.F.; Wallace, J.M. High Reynolds Number [$R_\theta = O(10^6)$] Boundary Layer Turbulence in the Atmospheric Surface Layer Above Western Utah’s Salt Flats. In *Flow at Ultra-High Reynolds and Rayleigh Numbers*; Springer: Berlin/Heidelberg, Germany, 1998; pp. 450–466.
6. Metzger, M.M.; Klewicki, J.C. A comparative study of near-wall turbulence in high and low Reynolds number boundary layers. *Phys. Fluids* **2001**, *13*, 692–701. [[CrossRef](#)]
7. Andreas, E.L.; Claffey, K.J.; Jordan, R.E.; Fairall, C.W.; Guest, P.S.; Persson, P.O.G.; Grachev, A.A. Evaluations of the von Kármán constant in the atmospheric surface layer. *J. Fluid Mech.* **2006**, *559*, 117–149. [[CrossRef](#)]
8. Marusic, I.; Kunkel, G.J. Streamwise turbulence intensity formulation for flat-plate boundary layers. *Phys. Fluids* **2003**, *15*, 2461–2464. [[CrossRef](#)]
9. Marusic, I.; Monty, J.P.; Hultmark, M.; Smits, A.J. On the logarithmic region in wall turbulence. *J. Fluid Mech.* **2013**, *716*, 1–11. [[CrossRef](#)]
10. Kunkel, G.J.; Marusic, I. Study of the near-wall-turbulent region of the high-Reynolds-number boundary layer using an atmospheric flow. *J. Fluid Mech.* **2006**, *548*, 375–402. [[CrossRef](#)]
11. Klewicki, J.C. Reynolds Number Dependence, Scaling, and Dynamics of Turbulent Boundary Layers. *J. Fluids Eng.* **2010**, *132*, 094001. [[CrossRef](#)]
12. Chen, X.; Sreenivasan, K.R. Reynolds number scaling of the peak turbulence intensity in wall flows. *J. Fluid Mech.* **2021**, *908*, R3. [[CrossRef](#)]
13. Chen, X.; Sreenivasan, K.R. Law of bounded dissipation and its consequences in turbulent wall flows. *J. Fluid Mech.* **2022**, *933*, A20. [[CrossRef](#)]
14. Lee, J.; Lee, H.J.; Kim, K.B.; Shin, H.H.; Lim, J.M.; Hong, J.; Lim, K.S.S. Height correction method based on the Monin–Obukhov similarity theory for better prediction of near-surface wind fields. *Atmos. Res.* **2023**, *292*, 106882. . [[CrossRef](#)]
15. Wyngaard, J.C. Atmospheric Turbulence. *Annu. Rev. Fluid Mech.* **1992**, *24*, 205–234. [[CrossRef](#)]
16. Foken, T. 50 Years of the Monin–Obukhov Similarity Theory. *Bound.-Layer Meteorol.* **2006**, *119*, 431–447. [[CrossRef](#)]
17. Liu, L.; Gadde, S.N.; Stevens, R.J.A.M. Universal Wind Profile for Conventionally Neutral Atmospheric Boundary Layers. *Phys. Rev. Lett.* **2021**, *126*, 104502. [[CrossRef](#)] [[PubMed](#)]
18. Prandtl, L. Meteorologische Anwendung der Stromungslehre. *Beitr. Phys. At.* **1932**, *19*, 188–202
19. Monin, A.S.; Obukhov, A.M. Basic laws of turbulent mixing in the ground of the atmosphere. *Dokl. Akad. Nauk SSSR* **1954**, *151*, 1963–1987.
20. Högström, U. Analysis of Turbulence Structure in the Surface Layer with a Modified Similarity Formulation for Near Neutral Conditions. *J. Atmos. Sci.* **1990**, *47*, 1949–1972. [[CrossRef](#)]
21. Högström, U. Review of some basic characteristics of the atmospheric surface layer. *Bound.-Layer Meteorol.* **1996**, *78*, 215–246. [[CrossRef](#)]
22. Priestley, C.H.B.; Panofsky, H.A. An alternative derivation of the diabatic wind profile. *Q. J. R. Meteorol. Soc.* **2010**, *87*, 437–438. [[CrossRef](#)]
23. Katul, G.G.; Konings, A.G.; Porporato, A. Mean velocity profile in a sheared and thermally stratified atmospheric boundary layer. *Phys. Rev. Lett.* **2011**, *107*, 268502. [[CrossRef](#)] [[PubMed](#)]
24. Businger, J.A. Flux profile relationships in the atmospheric surface layer. *J. Atmos. Sci.* **1971**, *28*, 181–189. [[CrossRef](#)]
25. Dyer, A.J. A review of flux-profile relationships. *Bound.-Layer Meteorol.* **1974**, *7*, 363–372. [[CrossRef](#)]
26. Carl, D.M.; Tarbell, T.C.; Panofsky, H.A. Profiles of Wind and Temperature from Towers over Homogeneous Terrain. *J. Atmos. Sci.* **1973**, *30*, 788–794. [[CrossRef](#)]

27. Kader, B.A.; Yaglom, A.M. Mean fields and fluctuation moments in unstably stratified turbulent boundary layers. *J. Fluid Mech.* **1990**, *212*, 637–662. [[CrossRef](#)]
28. Gioia, G.; Guttenberg, N.; Goldenfeld, N.; Chakraborty, P. Spectral theory of the turbulent mean-velocity profile. *Phys. Rev. Lett.* **2010**, *105*, 184501. [[CrossRef](#)]
29. Li, D.; Salesky, S.T.; Banerjee, T. Connections between the Ozmidov scale and mean velocity profile in stably stratified atmospheric surface layers. *J. Fluid Mech.* **2016**, *797*, R3. [[CrossRef](#)]
30. Liu, L.; Stevens, R.J.A.M. Vertical structure of conventionally neutral atmospheric boundary layers. *Proc. Natl. Acad. Sci. USA* **2022**, *119*, e2119369119. [[CrossRef](#)]
31. Salesky, S.T.; Anderson, W. Coherent Structures Modulate Atmospheric Surface Layer Flux-Gradient Relationships. *Phys. Rev. Lett.* **2020**, *125*, 124501. [[CrossRef](#)]
32. Stiperski, I.; Calaf, M. Generalizing Monin-Obukhov Similarity Theory (1954) for Complex Atmospheric Turbulence. *Phys. Rev. Lett.* **2023**, *130*, 124001. [[CrossRef](#)] [[PubMed](#)]
33. Ji, Y.; She, Z.S. Analytic derivation of Monin-Obukhov similarity function for open atmospheric surface layer. *Sci. China Phys. Mech. Astron.* **2021**, *64*, 34711. [[CrossRef](#)]
34. Chen, X.; Hussain, F. Similarity transformation for equilibrium boundary layers, including effects of blowing and suction. *Phys. Rev. Fluids* **2017**, *2*, 034605. [[CrossRef](#)]
35. She, Z.S.; Chen, X.; Hussain, F. Quantifying wall turbulence via a symmetry approach: A Lie group theory. *J. Fluid Mech.* **2017**, *827*, 322–356. [[CrossRef](#)]
36. Chen, X.; Hussain, F.; She, Z.S. Quantifying wall turbulence via a symmetry approach. Part 2. Reynolds stresses. *J. Fluid Mech.* **2018**, *850*, 401–438. [[CrossRef](#)]
37. She, Z.S.; Wu, Y.; Chen, X.; Hussain, F. A multi-state description of roughness effects in turbulent pipe flow. *New J. Phys.* **2012**, *14*, 093054. [[CrossRef](#)]
38. Wu, B.; Bi, W.; Hussain, F.; She, Z.S. On the invariant mean velocity profile for compressible turbulent boundary layers. *J. Turbul.* **2017**, *18*, 186–202. [[CrossRef](#)]
39. Jiménez, J. Cascades in Wall-Bounded Turbulence. *Annu. Rev. Fluid Mech.* **2012**, *44*, 27–45. [[CrossRef](#)]
40. Salesky, S.T.; Katul, G.G.; Chamecki, M. Buoyancy effects on the integral lengthscales and mean velocity profile in atmospheric surface layer flows. *Phys. Fluids* **2013**, *25*, 105101. [[CrossRef](#)]
41. Liu, H.; Wang, G.; Zheng, X. Amplitude modulation between multi-scale turbulent motions in high-Reynolds-number atmospheric surface layers. *J. Fluid Mech.* **2019**, *861*, 585–607. [[CrossRef](#)]
42. Liu, H.; Zheng, X. Large-scale structures of wall-bounded turbulence in single- and two-phase flows: Advancing understanding of the atmospheric surface layer during sandstorms. *Flow* **2021**, *1*, E5. [[CrossRef](#)]
43. Högström, U. Nondimensional wind and temperature profiles in the atmospheric boundary layer: A re-evaluation. *Bound.-Layer Meteorol.* **1988**, *42*, 55–78. [[CrossRef](#)]
44. Li, X.; Zimmerman, N.; Princevac, M. Local Imbalance of Turbulent Kinetic Energy in the Surface Layer. *Bound.-Layer Meteorol.* **2008**, *129*, 115–136. [[CrossRef](#)]

Disclaimer/Publisher’s Note: The statements, opinions and data contained in all publications are solely those of the individual author(s) and contributor(s) and not of MDPI and/or the editor(s). MDPI and/or the editor(s) disclaim responsibility for any injury to people or property resulting from any ideas, methods, instructions or products referred to in the content.